Chemical
Science

ROYAL SOCIETY
OF CHEMISTRY

EDGE ARTICLE

View Article Online
View Journal | View Issue

Check for updates

Cite this: *Chem. Sci.*, 2025, **16**, 22037

Manipulating spin-state conversion to promote asymmetric d–p orbital hybridization for high-efficiency nitrate electroreduction to ammonia

Ke Wang,†[a] Tong Zhao,†[a] Hou Wang, [b] Shiyu Zhang,[a] Rupeng Wang,[a] Meng Wang,[a] Zixiang He,[a] Nan-Qi Ren[a] and Shih-Hsin Ho *[a]

The electrochemical nitrate reduction reaction (eNO_3^-RR) presents a sustainable solution for water pollutant management and green ammonia (NH_3) synthesis. However, hindered by the spin-forbidden barrier, the sluggish hydrogenation kinetics of the key intermediate *NO severely limits the production of NH_3. Here, we reported for the first time the realization of a controllable transition of the inner Co spin-state from a low spin to a high spin in $CuCo_2O_4$ through the Mn doping-driven oxygen vacancy strategy ($Mn–CuCo_2O_{4-x}$). The elevated Co spin-state enhanced Co 3d ($d_{xz}/d_{yz}/d_{z^2}$)–*NO 2p asymmetrical orbital hybridization, facilitating *NO intermediate adsorption and the subsequent hydrogenation. Thanks to the Cu–Co synergistic effect enhanced *via* spin-state modulation, the $Mn–CuCo_2O_{4-x}$/graphene oxide aerogels (GAs) exhibited an attractive NH_3 yield rate of 2.14 mg h^{-1} cm^{-2} with a dramatic NH_3 faradaic efficiency of 98.37% at an environmentally relevant NO_3^- level (10 mM NO_3^-–N), far superior to that of Co_3O_4/GAs, $CuCo_2O_4$/GAs and as-reported catalysts. Moreover, the strong interfacial interaction between GAs and $Mn–CuCo_2O_{4-x}$ suppresses structural reconstruction of $Mn–CuCo_2O_{4-x}$, endowing the hybrid with robust stability. Herein, we confirm that spin-state modulation can enhance the Cu–Co synergistic effect and reveal a universal strategy to optimize intermediate adsorption/conversion through the spin-state, opening up a new avenue for deep purification of water pollutants based on spin optimization and providing general principles for the rational design of catalytic materials.

Received 4th September 2025
Accepted 24th September 2025

DOI: 10.1039/d5sc06823a

rsc.li/chemical-science

1. Introduction

Increasingly serious problems of nitrogen cycle disruption and environmental contamination pose significant threats to the global ecosystem and public health.[1–3] Nitrate (NO_3^-), a predominant contaminant in industrial effluents and agricultural runoff, is identified as a critical contributor to eutrophication, drinking water pollution and ecosystem disruption.[4,5] Concurrently, ammonia (NH_3) serves as the core raw material for agricultural fertilizers and clean hydrogen energy carriers. The conventional NH_3 production method depends on the energy-consuming Haber–Bosch process, generating a considerable carbon footprint.[6,7] The electrochemical nitrate reduction reaction (eNO_3^-RR) can convert NO_3^- into value-added NH_3 under mild conditions, providing a sustainable solution to the above dual challenges.[8–10] Despite its promise, the practical implementation of the eNO_3^-RR is fundamentally throttled by the kinetically sluggish hydrogenation of a critical intermediate (*NO), where a spin-forbidden barrier imposes severe limitations on reaction rates and faradaic efficiency (FE).

The hydrogenation of *NO constitutes the rate-determining step (RDS) in the eNO_3^-RR, as its spin-polarized triplet ground state inherently resists forming singlet *HNO intermediates—a classic manifestation of spin selection rules. The Cu–Co bimetallic system in the eNO_3^-RR partially mitigates this kinetic barrier through functional decoupling, in which the Cu site preferentially adsorbs NO_3^- and drives the initial deoxygenation reaction and the Co site is responsible for the subsequent *NO hydrogenation conversion.[11–13] However, current design paradigms predominantly focus on macro/meso-structure engineering (*e.g.*, alloying, defect modulation, and reconstruction).[14–16] These approaches fail to deeply modulate the essential electronic structure determinants. As a core feature of the d-orbital electron arrangement of transition metals, the spin-state can significantly change the orbital adsorption strength and hybridization mode of metal intermediates, thereby impacting the reaction process.[17] Spinel-type $CuCo_2O_4$ is an ideal platform for resolving the Co spin-state effect due to its unique structural tunability. Co^{3+} occupies

---

[a] *State Key Laboratory of Urban Water Resource and Environment, School of Environment, Harbin Institute of Technology, Harbin, 150040, P. R. China. E-mail: stephen6949@hit.edu.cn*

[b] *College of Environmental Science and Engineering and Key Laboratory of Environmental Biology and Pollution Control (Ministry of Education), Hunan University, Changsha, 410082, China*

† These authors contributed equally to this work.

the octahedral site in $CuCo_2O_4$, and its spin-state is significantly affected by the local coordination environment and lattice stresses.[18] Some studies have shown that by introducing heteroatoms for doping in Co-based materials to induce lattice distortions, the ligand field strength of Co^{3+} can be effectively tuned, consequently enabling controllable switching of the spin-state.[19–21]

The spin-state of Co sites critically determines the d-orbital energy level configuration, where the HS state exhibits stronger ligand field splitting effects and higher occupancy in the e_g orbitals.[22,23] This electronic configuration enhances the adsorption and activation of reaction intermediates through optimized orbital interactions, thereby facilitating the RDS in catalytic processes.[24] Notably, compelling theoretical and experimental validation for such spin-dependent electronic modulation effects exists in analogous spin-sensitive electrochemical processes, such as the oxygen reduction and evolution reactions, yet this potent strategy remains conspicuously unexplored and underutilized within the eNO_3^-RR framework.[25,26] Consequently, it is imperative to elucidate whether HS Co sites can indeed enhance *NO adsorption and accelerate its hydrogenation kinetics through changing the orbital hybridization pattern with the *NO intermediate and to unravel the interplay between the Co spin-state and the established Cu–Co synergistic effect. These interesting validations will unlock unprecedented activity and selectivity for next generation NO_3^- reduction electrocatalysts.

Here, we utilized $CuCo_2O_4$ as a model catalytic system and proposed a Mn doping-driven oxygen vacancy strategy to precisely modulate the spin-state of Co. Experimental studies demonstrate that the HS state Co can greatly optimize the adsorption of *NO and solve the problem of slow hydrogenation kinetics in the RDS (*NO → *HNO) *via* enhancing the asymmetric hybridization of the Co 3d ($d_{xz}/d_{yz}/d_{z^2}$)–*NO 2p orbitals. This spin state-optimized bimetallic synergistic effect endowed $Mn–CuCo_2O_{4-x}$/GAs with excellent catalytic performance (Faradaic Efficiency (FE): 98.37%, yield rate: 2.14 mg h^{-1} cm^{-2} at −0.6 V *vs.* RHE, and 10 mM NO_3^-–N), exceeding that of Co_3O_4/GAs, $CuCo_2O_4$/GAs and as-reported catalysts. This work provides a theoretical paradigm for extending the spin-engineering strategy to bimetallic synergistic catalytic systems, while also inaugurating a new dimension of electronic structure modulation for designing efficient NO_3^- conversion catalysts.

2. Experimental section

2.1 Chemicals

All chemical reagents are depicted in Text S1.

2.2 Catalyst preparation

2.2.1 Preparation of GAs. Graphene aerogels (GAs) were synthesized by a hydrothermal combined calcination method. A standard synthesis protocol involved homogenizing 60 mg carboxymethyl cellulose (CMC) with 30 mL graphene oxide (GO) (2 mg mL^{-1}) under ultrasonic processing for 60 min. This precursor solution underwent hydrothermal treatment at 180 °C for 12 h. The synthesized hydrogels were purified using deionized water, freeze-dried, and then thermally treated at 900 °C for 2 h under N_2 flow to generate GAs. Finally, the GAs were functionalized with 0.2 mL aminopropyltriethoxysilane (APTES) to impart a positive surface charge.

2.2.2 Preparation of $Mn–CuCo_2O_{4-x}$ yolk–shell spheres. A blend of $Cu(NO_3)_2\cdot3H_2O$ (0.1 mmol), $Co(NO_3)_2\cdot6H_2O$ (0.2 mmol), a certain amount of $Mn(NO_3)_2\cdot6H_2O$, and 8 mL glycerol was introduced into 40 mL isopropanol and stirred to obtain homogeneous solution. This solution was moved into a 100 mL solvothermal reaction vessel lined with Teflon and maintained at a temperature of 180 °C over 6 h. The resulting precursor from the solvothermal reaction was subjected to a dual centrifugal rinse using deionized water and ethanol before undergoing a 12 h drying phase at 80 °C. The $Mn–CuCo_2O_{4-x}$ yolk–shell spheres were then generated by placing the dried precursor in a tube furnace set at 400 °C and sustained for 1 h under O_2 conditions. Co_3O_4 and $CuCo_2O_4$ were prepared similarly to $Mn–CuCo_2O_{4-x}$ except that the corresponding metal salts were not added.

2.2.3 Preparation of $Mn–CuCo_2O_{4-x}$/GAs. The $Mn–CuCo_2O_{4-x}$/GAs composite was self-assembled from GAs and $CuCo_2O_4$. More specifically, an initial step involves dispersing 0.1 g $Mn–CuCo_2O_{4-x}$ yolk–shell spheres in an isopropanol solution loaded with poly(sodium 4-styrenesulfonate) (PSS) (concentration: 0.2 mL PSS and 20 mL isopropanol), yielding PSS-treated $Mn–CuCo_2O_{4-x}$ yolk–shell spheres. These spheres were subsequently cleaned twice by centrifugation using alcohol and deionized water. The cleaned product was then dispersed in deionized water and gently added to a GA suspension (60 mL, 0.5 mg mL^{-1}) and stirred for 180 min to achieve a dispersion of $Mn–CuCo_2O_{4-x}$/GAs composite material. The $Mn–CuCo_2O_{4-x}$/GAs composite material was isolated *via* vacuum filtration and sequentially purified with ethanol-aqueous solution under ambient conditions. Co_3O_4/GAs and $CuCo_2O_4$/GAs were prepared by the same procedure as that of $Mn–CuCo_2O_{4-x}$/GAs.

2.2.4 The preparation of the working electrode. 10 mg of the catalysts were re-dispersed into 470 μL of ethanol and 470 μL of deionized water, followed by adding 60 μL of Nafion solution to make a homogeneous solution. Subsequently, it was ultrasonicated for about 1 h to enable the good dispersion of catalyst inks. Afterwards, 100 μL of catalyst inks were dropped onto the carbon paper with an area of 1 cm^2 (1 cm × 1 cm).

2.3 Characterization

More details on the characterization methods are provided in the SI (Text S2).

2.4 Electrochemical measurements

Electrochemical tests were performed using a three-electrode system connected to a CHI 760E electrochemical workstation in a typical H-cell. The H-cell was separated using a Nafion 117 membrane (Dupont) that was pretreated following reported procedures. The catalysts were used as the working electrode, while an Ag/AgCl electrode and platinum mesh were used as the reference and counter electrodes, respectively. The electrolytes were Ar-saturated 0.1 M Na_2SO_4 containing 10 mM NO_3^-–N. All potentials were calibrated to the reversible hydrogen electrode (RHE) scale using the Nernst equation ($E_{RHE} = E_{Ag/AgCl} + 0.197$ V + 0.059 V × pH). The current density was normalized to the geometric electrode area (~1 cm^2). The linear sweep voltammetry (LSV) test was carried out in a three-electrode system at scanning rates of 10 mV s^{-1}. Electrochemical impedance spectroscopy (EIS) measurements were conducted in a frequency range from 10^5 to 0.01 Hz with 5 mV amplitude. Cyclic voltammetry (CV) curves were obtained in the non-faradaic region with different scan rates (20, 40, 60, 80, and 100 mV s^{-1}).

2.5 Analytical methods

Detailed information of nitrogen species concentration determination and the calculation of the eNO_3^-RR parameters are provided in Text S3 and S4, respectively. Detailed steps of *in situ* Fourier transform infrared spectroscopy (FT-IR), online differential electrochemical mass spectrometry (DEMS), and electron spin resonance (ESR) measurements are described in Text S5–S7, respectively. Density functional theory (DFT) calculations are presented in Text S8.

3. Results and discussion

3.1 Catalyst characterization

The preparation process of the Mn–$CuCo_2O_{4-x}$/GAs composite framework is shown in Fig. 1a. First, Mn–$CuCo_2O_{4-x}$ yolk–shell nanospheres were prepared *via* solvothermal combined high-temperature calcination. Subsequently, Mn–$CuCo_2O_{4-x}$/GAs was synthesized *via* a charge neutralization process. A thorough examination of the microstructure of Mn–$CuCo_2O_{4-x}$ was conducted using scanning electron microscopy (SEM) and transmission electron microscopy (TEM). Mn–$CuCo_2O_{4-x}$ possessed a well-defined yolk–shell architecture, as clearly observed in Fig. 1b and c, characterized by an average particle diameter of approximately 400 nm and distinct surface roughness. Selected area electron diffraction (SAED) analysis confirmed the polycrystalline characteristics of Mn–$CuCo_2O_{4-x}$ (Fig. 1d). Elemental mapping *via* energy-dispersive spectroscopy (EDS) confirmed homogeneous spatial distribution of Mn, Cu, Co, and O constituents throughout the yolk–shell spheres (Fig. 1e–i). Inductively coupled plasma mass spectrometry (ICP-MS) quantified Mn content at 9.36 wt% (Table S1). The combined results from EDS and ICP-MS analysis conclusively verified the successful incorporation of Mn within the composite structure. The Mn–CuCo glycerate precursors underwent structural evolution into yolk–shell architectures *via* the Ostwald maturation mechanism, as also supported *via* comparative TEM analyses of Co_3O_4 and $CuCo_2O_4$ phases (Fig. S1–S4).[27] To impart Mn–$CuCo_2O_{4-x}$ with negative electrical properties, we utilized PSS for its modification *via* electrostatic self-assembly. During the PSS modification process, the sulfonic acid group (SO_3^-) of PSS was adsorbed on the surface of Mn–$CuCo_2O_{4-x}$ through electrostatic interaction, forming a stable negatively charged layer (Fig. S5).[28] Simultaneously, the amino group ($-NH_2$) of the APTES molecule underwent a protonation reaction with protons in solution to form positively charged ammonium ions ($-NH_3^+$), and $-NH_3^+$ was stably anchored to the surface of the GAs *via* covalent bonds, thus conferring a positively charged character.[29] Then, the oppositely charged Mn–$CuCo_2O_{4-x}$ and GAs were mixed to form the Mn–$CuCo_2O_{4-x}$/GAs composites *in situ* through a charge neutralization process. As illustrated in Fig. 1j and k, Mn–$CuCo_2O_{4-x}$ was embedded into the 3D porous skeleton of GAs to form a stable Mn–$CuCo_2O_{4-x}$/GAs composite framework. The introduction of GAs promoted rapid electron transport while effectively maintaining the stability of the structure, as will be detailed in the subsequent stability characterization section. High-resolution TEM (HRTEM) images demonstrated clear lattice streaks and GA layers, and the measured crystal plane spacing of 0.245 nm corresponded to the (311) crystal plane of $CuCo_2O_4$, confirming that the spinel structural features were maintained after Mn doping (Fig. 1l). TEM images of Co_3O_4/GAs and $CuCo_2O_4$/GAs composites suggested that Co_3O_4 and $CuCo_2O_4$ were also tightly coupled to the GA scaffolds, thus confirming the general applicability of the charge neutralization strategy in constructing metal oxide/GAs composites (Fig. S6 and S7).

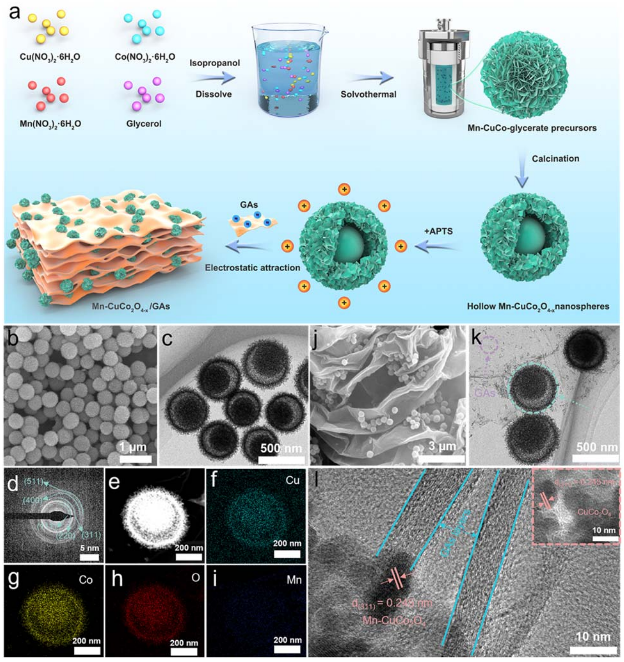

Fig. 1 (a) The synthesis schematic of Mn–$CuCo_2O_{4-x}$/GAs. (b) SEM, (c) TEM, (d) SAED, and (e–i) elemental mapping of Mn–$CuCo_2O_{4-x}$. (j) SEM, (k) TEM, and (l) HRTEM images of Mn–$CuCo_2O_{4-x}$/GAs (inset: HRTEM images of Mn–$CuCo_2O_{4-x}$).

The successful synthesis of the $CuCo_2O_4$ spinel-type framework was confirmed by the X-ray diffraction (XRD) analysis showing consistent crystallographic diffraction peaks at (220), (311), (400), (422), (440), and (533) with the standard card (PDF#78-2177) (Fig. 2a).[30] After Mn doping, the diffraction peaks all exhibited a systematic shift to the low angle direction, among which the displacement of the (311) crystal plane was the most significant, originating from the lattice expansion

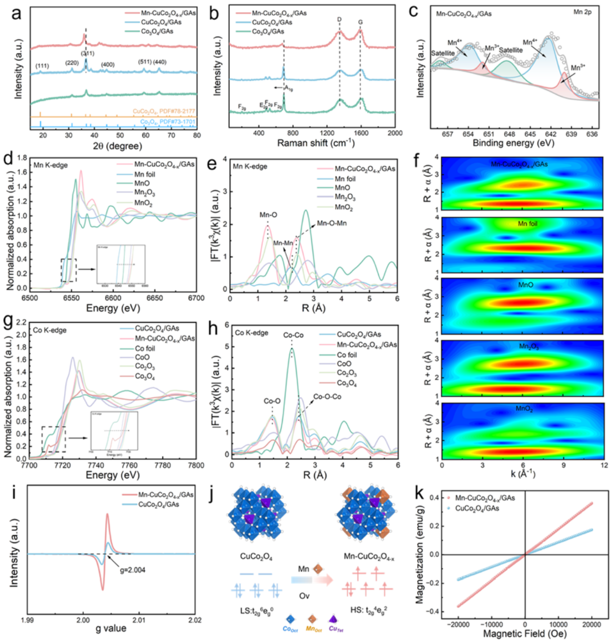

Fig. 2 (a) XRD and (b) Raman spectra of Co_3O_4/GAs, $CuCo_2O_4$/GAs, and Mn–$CuCo_2O_{4-x}$/GAs. (c) High-resolution XPS images of Mn 2p of Mn–$CuCo_2O_{4-x}$/GAs. (d) Mn K-edge XANES spectra of Mn–$CuCo_2O_{4-x}$/GAs and the standard reference materials, and (e) their corresponding FT-EXAFS spectra. (f) Mn K-edge WT-EXAFS contour plots for Mn–$CuCo_2O_{4-x}$/GAs, Mn foil, MnO, Mn_2O_3 and MnO_2. (g) Co K-edge XANES spectra of $CuCo_2O_4$/GAs and Mn–$CuCo_2O_{4-x}$/GAs and the standard reference materials, and (h) their corresponding FT-EXAFS spectra. (i) EPR images of $CuCo_2O_4$/GAs and Mn–$CuCo_2O_{4-x}$/GAs; (j) the influence of Ov on the electron occupancy of Co 3d orbitals. (k) Magnetic hysteresis loops of $CuCo_2O_4$/GAs and Mn–$CuCo_2O_{4-x}$/GAs.

triggered by the difference in ionic radii between Mn and Co. A weakening of the diffraction peak intensity and a slight broadening of the half height width were also observed, suggesting that the doping process may lead to a decrease in crystallinity. The Raman analysis of $CuCo_2O_4$ exhibited characteristic peaks at about 475, 521, 627, and 684 cm^{-1} attributed to the E_{2g}, F_{2g}, and A_{1g} vibrational modes of the CoO_6 octahedron (Fig. 2b).[31] Since there is a spectral overlap between the F_{2g} vibrational mode of the CuO_4 tetrahedron (190 cm^{-1}) and the F_{2g} vibrational mode of the tetrahedral CoO_4 tetrahedron (195 cm^{-1}), the characteristic signals of the CuO_4 tetrahedron were not effectively recognized.[32,33] The Raman peak of A_{1g} in $CuCo_2O_4$ was shifted toward the low wave number direction, which originated from the lattice substitution effect of the CoO_6 octahedron by the MnO_6 octahedron with a larger radius. The larger ionic radius can induce local lattice distortion, leading to an increase in metal–oxygen bond length and structural stress, which is consistent with the theoretical model of cation substitution-induced bond length rearrangement.[34] Meanwhile, the characteristic vibrational modes of the D and G bands of the graphitic carbon layer of GAs were detected in Raman spectra, confirming the effective coupling of $CuCo_2O_4$ to GAs.

The chemical valence and coordination environments of the elements were characterized using X-ray photoelectron spectroscopy (XPS) analysis. The XPS full spectra revealed characteristic peaks associated with Mn–$CuCo_2O_{4-x}$ and GAs, indicating the successful construction of $CuCo_2O_4$ and GA composites (Fig. S8). The high-resolution XPS spectra of the Cu 2p orbital presented characteristic double peaks at 933.9 eV ($2p_{3/2}$) and 954.0 eV ($2p_{1/2}$), confirming that the Cu element exists in the +2-valence state in $CuCo_2O_4$ and Mn–$CuCo_2O_{4-x}$ (Fig. S9).[32] Remarkably, the doping of Mn did not change the chemical state of Cu since the binding energy positions and ratios of the two orbitals were not changed. The high-resolution XPS spectra of the Mn 2p orbital were divided into Mn $2p_{3/2}$ and Mn $2p_{1/2}$, and the predominant oxidation state of Mn in the samples was Mn^{4+} (Fig. 2c).[35] The Co 2p orbital of $CuCo_2O_4$ exhibited double state features at 779.7/781.5 eV ($2p_{3/2}$) and 796.6/794.7 eV ($2p_{1/2}$), confirming that Co^{2+} and Co^{3+} coexist in the material, and Co^{3+} occupies the main component (Fig. S10).[32,36] Notably, the decrease in the Co^{3+}/Co^{2+} ratio in Mn–$CuCo_2O_{4-x}$ confirmed the preferential occupation of CoO_6 octahedral sites by Mn^{4+}. The O 1s orbitals presented peaks at 529.6, 531.1, and 532.6 eV, corresponding to metal–oxygen (M–O), Ov, and H_2O, respectively, and the Ov concentration of Mn–$CuCo_2O_{4-x}$ was higher than that of $CuCo_2O_4$ (Fig. S11).[37] X-ray absorption spectroscopy (XAS) elucidated the electronic state and local coordination of metal elements. Based on the linear combination fitting of the absorption edge positions (Fig. 2d and S12a), the oxidation state of Mn in Mn–$CuCo_2O_{4-x}$ was found to be +3.8, which is consistent with the XPS results. Extended X-ray absorption fine structure (EXAFS) analysis of the Mn K-edge (Fig. 2e and S13) revealed no evidence of the Mn–Mn bond, confirming the atomic dispersion of Mn and absence of clusters. The wavelet transform (WT) spectroscopy in *R*-space (Fig. 2f) of Mn foil, MnO, Mn_2O_3, MnO_2, and Mn–$CuCo_2O_{4-x}$ demonstrated spectral similarity between Mn–$CuCo_2O_{4-x}$ and octahedrally coordinated MnO_2. These results confirm an octahedral coordination environment for Mn, supporting its primary substitution at octahedral Co sites. The normalized Co K-edge X-ray absorption near-edge structure (XANES) spectra (Fig. 2g and S12b) of $CuCo_2O_4$ was located between Co_3O_4 and Co_2O_3, but closer to Co_2O_3, indicating that Co was predominantly +3 valence in $CuCo_2O_4$. In contrast, the Co K-edge XANES spectra of Mn–$CuCo_2O_{4-x}$ were shifted towards lower energy, suggesting that the substitution of Co^{3+} by Mn^{4+} leads to an increase in the Co^{2+} ratio. Co K-edge EXAFS analysis (Fig. 2g) revealed a significant reduction in oscillation amplitude for Mn–$CuCo_2O_{4-x}$ compared to pristine $CuCo_2O_4$, indicative of increased local structural disorder around Co atoms induced by the incorporation of high-valent Mn^{4+} ions. Both the Co K-edge EXAFS spectra of $CuCo_2O_4$ and Mn–$CuCo_2O_{4-x}$ and their corresponding R-space WT spectra (Fig. S14 and S15) show no evidence of Co–Co bonding contributions. Moreover, the EXAFS fitting result (Table S2) of the first-shell peak for $CuCo_2O_4$ and Mn–$CuCo_2O_{4-x}$ revealed that the introduction of Ov reduces the average coordination number of Co.

Prior research has indicated that the addition of metal doping can create lattice distortions and reduce the strength of the metal–oxygen bond, thereby promoting the creation of oxygen vacancies (Ov).[38] Consequently, we analyzed the variations in the Ov concentration in the samples using electron paramagnetic resonance (EPR) tests. Compared with $CuCo_2O_4$/GAs, Mn–$CuCo_2O_{4-x}$/GAs exhibited significantly enhanced signal intensity in EPR spectra, confirming the elevated Ov concentration (Fig. 2i). Since Ov are positively charged defects, they would release free electrons into the surroundings to maintain electrical neutrality. These electrons can be trapped by neighboring Co^{3+} to form transient Co^{2+}, enhancing the spin-state of Co^{3+}. In the pristine $CuCo_2O_4$, Co^{3+} is usually in a LS state ($t_{2g}{}^6e_g{}^0$) with a high octahedral coordination field splitting energy, and the electrons preferentially populate the t_{2g} orbitals in the lower energy levels (Fig. 2j). The introduction of Ov induces localized lattice distortion. This structural alteration further modifies the coordination environment of transition metal ions, causing their coordination field splitting energy to fall below the critical threshold. At this point, Co^{3+} transitions from the LS state to the HS state ($t_{2g}{}^4e_g{}^2$), and the number of unpaired electrons increases to four. To validate the proposed introduction of Ov altering the Co^{3+} spin-state, we measured sample magnetism *via* vibrating sample magnetometry. As displayed in Fig. 2k, original $CuCo_2O_4$ exhibited a weak saturation magnetization intensity whereas the saturation magnetization intensity was significantly increased by the introduction of Ov. This phenomenon indicated that Ov may induce the transition of Co^{3+} from the LS to the HS state through modulation of the localized crystal field and electron occupation, leading to a larger number of spin electrons. In summary, Ov can significantly enhance the number of spin-polarized electrons *via* triggering the HS state transition of Co^{3+}, promoting a more effective “spin promoter” for the orbital interaction between the catalyst and the *NO intermediate.

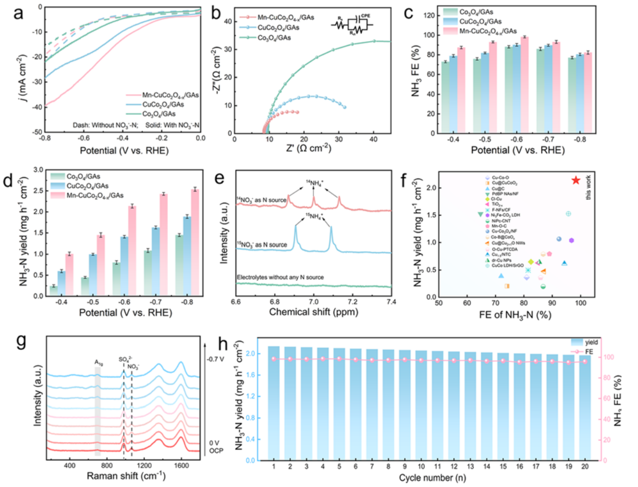

Fig. 3 (a) LSV curves, (b) EIS curves, (c) FE, and (d) NH_3–N yield rates of Co_3O_4/GAs, $CuCo_2O_4$/GAs, and Mn–$CuCo_2O_{4-x}$/GAs. (e) ^1H NMR spectra for $^{14}NO_3{}^-$ and $^{15}NO_3{}^-$ electrolyte after 1 h of electrolysis. (f) Comparison of $eNO_3{}^-RR$ performance of Mn–$CuCo_2O_{4-x}$/GAs with that of reported electrocatalysts. (g) *In situ* Raman spectra of Mn–$CuCo_2O_{4-x}$/GAs at different voltages. (h) The cycling stability tests of Mn–$CuCo_2O_{4-x}$/GAs.

3.2 Electrocatalytic performance for the $NO_3{}^-RR$

The electrocatalytic activities of Co_3O_4/GAs, $CuCo_2O_4$/GAs, and Mn–$CuCo_2O_{4-x}$/GAs were assessed in an H-type cell. $NO_3{}^-$, $NO_2{}^-$, and $NH_4{}^+$ concentrations during the $eNO_3{}^-RR$ were quantified *via* UV-Vis spectrophotometry (Fig. S16–S18). The linear sweep voltammetry (LSV) curves revealed enhanced current densities for Co_3O_4/GAs, $CuCo_2O_4$/GAs, and Mn–$CuCo_2O_{4-x}$/GAs *versus* $NO_3{}^-$-free systems, confirming their intrinsic $NO_3{}^-$ reduction activity (Fig. 3a). Notably, $CuCo_2O_4$/GAs exhibited higher current density than Co_3O_4/GAs, implicating synergistic advantages of Cu–Co bimetallic sites in the $eNO_3{}^-RR$. Additionally, Mn–$CuCo_2O_{4-x}$/GAs possessed higher current density and more positive starting reduction potential compared with $CuCo_2O_4$/GAs, suggesting that Mn doping further can enhance the catalytic activity of the $eNO_3{}^-RR$. Electrochemical impedance spectrum (EIS)-based analysis of electron transport kinetics showed that Mn–$CuCo_2O_{4-x}$/GAs possessed the smallest capacitive arc radius in the Nyquist plot (Fig. 3b). Moreover, the R_{ct} values showed a dramatic and conclusive trend: Co_3O_4/GAs (66.17 Ω) > $CuCo_2O_4$/GAs (26.69 Ω) > Mn–$CuCo_2O_{4-x}$/GAs (15.64 Ω), which was in excellent agreement with the observed catalytic activity (Table S3). This decrease in R_{ct} unequivocally demonstrated that the charge transfer kinetics for the $eNO_3{}^-RR$ was significantly enhanced upon introducing Cu, indicating that the bimetallic synergy drastically facilitated the electron transfer process. Most impressively, Mn–$CuCo_2O_{4-x}$/GAs achieved the lowest R_{ct} value, which provided direct electrochemical evidence that the Mn doping and the induced Ov created a more favorable electronic structure, further accelerating the rate-determining electron transfer steps in the $eNO_3{}^-RR$. Electrochemical active surface area (ECSA) was quantified by electrochemical double-layer capacitance (C_{dl}) measurements from cyclic voltammetry (CV) in non-faradaic windows (Fig. S19). A higher C_{dl} value was obtained for Mn–$CuCo_2O_{4-x}$/GAs (5.20 mF cm^{-2}) *versus* Co_3O_4/GAs (1.62 mF cm^{-2}) and $CuCo_2O_4$/GAs (2.22 mF cm^{-2}), confirming that Cu–Co bimetallic synergism together with Mn doping can increase the active site density, thus enhancing the intrinsic activity of the $eNO_3{}^-RR$. Based on the LSV results, −0.4 to −0.8 V *vs.* RHE was identified as the characteristic potential window. The chronoamperometry quantified the FE and NH_3–N yield rates of catalysts (Fig. S20). The trend of volcanic distribution of FE for each catalyst confirmed the existence of a critical starting overpotential for the $eNO_3{}^-RR$ (Fig. 3c). Excessively negative potentials attenuated FE due to the competing hydrogen evolution reaction (HER). Mn–$CuCo_2O_{4-x}$/GAs exhibited higher FE than both counterparts across tested potentials, achieving a maximum of 98.37% at −0.6 V *vs.* RHE. Mn–$CuCo_2O_{4-x}$/GAs presented the highest NH_3–N yield rate at all potentials; especially at the voltage corresponding to the optimal FE, the NH_3-N yield rate was 2.14 mg h^{-1} cm^{-2} (Fig. 3d). Additionally, the selectivity of the catalysts was further evaluated based on the yield rate and FE of the intermediate $NO_2{}^-$ (Fig. S21). As the applied voltage increased, both the $NO_2{}^-$ yield rate and corresponding FE of the three catalysts exhibited a gradual decrease. Among them, Mn–$CuCo_2O_{4-x}$/GAs maintained the lowest values for both metrics, indicating its greater ability to promote the further conversion of the intermediate NO_2^-. This highlights the outstanding selectivity of this catalyst in the NO_3^- reduction process.

The properties of the nitrogen source in NH_3–N were verified through a blank control. The results revealed almost negligible ammonia production in the blank control, clearly confirming that the nitrogen in the product originated from NO_3^- rather than from environmental pollutants (Fig. S22). ^{1}H-nuclear magnetic resonance (^{1}H-NMR) was used to monitor the dynamics of the nitrogen conversion pathways. When $^{15}NO_3^-$ and $^{14}NO_3^-$ were employed as nitrogen sources, the corresponding $^{15}NH_4^+$ and $^{14}NH_4^+$ showed characteristic double-peak and triple-peak splitting patterns, providing direct evidence for the directional conversion of NO_3^- to NH_3 (Fig. 3e). Although Mn–$CuCo_2O_{4-x}$/GAs had excellent catalytic activity, the performance comparison between this material and similar advanced catalysts still needs to be clarified. To this end, we systematically summarized the recent literature for the low-concentration NO_3^- system (Fig. 3e and Table S4). Both the FE and NH_3–N yield rate of Mn–$CuCo_2O_{4-x}$/GAs were significantly better than those of other reported systems, fully demonstrating the leading position of this catalyst in the eNO_3^-RR. The structural evolution of the Mn–$CuCo_2O_{4-x}$/GAs electrocatalyst during the eNO_3^-RR was dynamically tracked using *in situ* Raman spectroscopy. In the absence of GAs, the characteristic Raman peak corresponding to the A_{1g} vibrational mode of Mn–$CuCo_2O_{4-x}$ exhibited a rapid decrease in intensity as the applied potential shifted negatively, indicating insufficient structural stability under operating conditions (Fig. S23). In contrast, after the introduction of GAs, the same characteristic Raman mode remained clearly detectable even at highly negative potentials up to −0.7 V *vs.* RHE, demonstrating significantly enhanced structural integrity (Fig. 3g). This pronounced contrast underscores the critical role of GAs in stabilizing the active material through strong interfacial interactions, which effectively anchor Mn–$CuCo_2O_{4-x}$, prevent agglomeration or dissolution, and thus maintain the structural and catalytic durability of the Mn–$CuCo_2O_{4-x}$/GAs composite throughout the reaction. The FE and NH_3–N yield rate of the system exhibited only minor fluctuations during the continuous electrolysis test for up to 20 h, demonstrating excellent cycling stability (Fig. 3h). The catalysts before and after the reaction were systematically characterized by XRD and TEM, and neither the crystal structure nor the microscopic morphology significantly changed, further verifying the excellent structural stability of Mn–$CuCo_2O_{4-x}$/GAs at the microscopic level (Fig. S24 and S25).

3.3 Reaction pathways and mechanisms

Time-resolved electrochemical mass spectrometry (DEMS) identified key eNO_3^-RR intermediates on $CuCo_2O_4$/GAs and Mn–$CuCo_2O_{4-x}$/GAs (Fig. 4a, b and S26). *m*/*z* signals at 15, 16, 17, 30, and 31 revealed *NH, *NH_2, *NO, HNO, and NH_3 intermediate generation. Notably, the characteristic signal peak intensity of the relevant intermediates on Mn–$CuCo_2O_{4-x}$/GAs was significantly higher than that on $CuCo_2O_4$/GAs, suggesting that the introduction of Ov can significantly enhance the generation capacity of the key intermediates. *Operando* Fourier transform infrared spectroscopy (FT-IR) tracked real-time evolution of surface intermediates during the reaction (Fig. 4c and S27). The vibrational peaks at 1650 cm^{-1} (δH–O–H) and 3300 cm^{-1} (νH–O–H) corresponded to interfacial water adsorption and cleavage.[39,40] The progressive intensification of vibrational signatures at 1460 cm^{-1} and 3200 cm^{-1} can be unambiguously assigned to the stretching vibrations of N–H bonds in NH_3 molecules.[41,42] Based on the key intermediate species and their dynamic evolution patterns monitored online in this study, combined with the mechanistic models reported in the literature, we systematically deduced and constructed the reaction pathway dominated by the stepwise hydrogenation of *NO (Fig. S28). The dynamic evolutionary behavior of active hydrogen species (*H) during the eNO_3^-RR process was systematically investigated by the *in situ* EPR technique (Fig. 4d). The 5,5-dimethyl-1-pyrroline-N-oxide (DMPO)–*H spin adduct signal intensity for Mn–$CuCo_2O_{4-x}$/GAs doubled that of $CuCo_2O_4$/GAs in 0.1 M Na_2SO_4 electrolyte lacking NO_3^-, confirming that Mn doping effectively promoted hydrolytic dissociation to generate *H. Intriguingly, upon introducing 10 mM NO_3^- into the electrolyte, the characteristic signal intensity

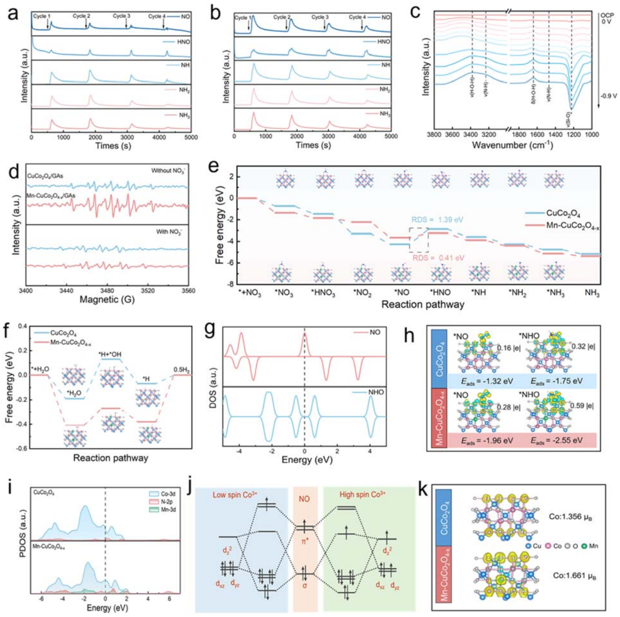

Fig. 4 (a and b) Online DEMS spectra of $CuCo_2O_{4-x}$/GAs and Mn–$CuCo_2O_{4-x}$/GAs. (c) *In situ* FT-IR spectra of Mn–$CuCo_2O_{4-x}$/GAs. (d) EPR spectra of $CuCo_2O_{4-x}$/GAs and Mn–$CuCo_2O_{4-x}$/GAs in electrolytes without/with NO_3^-. Gibbs free energy profiles for (e) eNO_3^-RR and (f) HER on $CuCo_2O_4$ and Mn–$CuCo_2O_{4-x}$. (g) DOS of *NO and *HNO species. (h) Differential charge density of critical intermediates adsorbed on $CuCo_2O_4$ and Mn–$CuCo_2O_{4-x}$ interfaces. (i) PDOS analyses of *NO intermediates adsorbed on $CuCo_2O_4$ and Mn–$CuCo_2O_{4-x}$. (j) Schematic illustration of orbital hybridization of Co and *NO in different spin states. (k) Spin charge density of $CuCo_2O_4$ and Mn–$CuCo_2O_{4-x}$.

corresponding to the *H on Mn–$CuCo_2O_{4-x}$/GAs exhibited significant attenuation during the electrocatalytic process. This apparent inhibitory effect may stem from the rapid depletion caused by *H and NO_3^- reactions. These findings demonstrate that NO_3^- reduction on Mn–$CuCo_2O_{4-x}$/GAs proceeded *via* an *H-mediated indirect pathway and the Ov promoted the hydrogenation process of nitrogen-containing intermediates. To further evaluate the interfacial H_2O dissociation capability of the prepared catalysts, kinetic isotope effect (KIE) tests were conducted by replacing H_2O with D_2O. The KIE value was calculated by comparing the current densities measured in H_2O and D_2O, thereby revealing the dynamic process of *H transfer during H_2O dissociation (Fig. S29). The results indicated that Mn–$CuCo_2O_{4-x}$/GAs exhibits an average KIE value of 1.24, significantly lower than that of other reference electrocatalysts, demonstrating that the introduction of Ov effectively promotes interfacial H_2O dissociation. Concurrently, it also demonstrated that Ov possesses a significant interface water regulation behavior. Gibbs free energy change (ΔG) plots for $CuCo_2O_4$ and Mn–$CuCo_2O_{4-x}$ in the eNO_3^-RR are shown in Fig. 4e. Both $CuCo_2O_4$ and Mn–$CuCo_2O_4$ synthesize NH_3 *via* the 8-electron reduction pathway ($NO_3^- \rightarrow *NO_3 \rightarrow *HNO_3 \rightarrow *NO_2 \rightarrow *NO \rightarrow *HNO \rightarrow *NH \rightarrow *NH_2 \rightarrow *NH_3 \rightarrow NH_3$) (Fig. S30 and S31). The ΔG profile identified *NO hydrogenation to *HNO as the rate-determining step (RDS), exhibiting the highest energy barrier. Apparently, Ov lowered the RDS energy barrier from 1.39 eV to 0.41 eV, thereby enhancing eNO_3^-RR kinetics. Promoting the dissociation of H_2O to produce *H and inhibiting the coupling of *H to produce H_2 are essential to enhance the performance of the eNO_3^-RR. As illustrated in Fig. 4f, S32 and S33, the H_2O adsorption energy of Mn–$CuCo_2O_{4-x}$ (−0.41 eV) was significantly negatively shifted compared with that of $CuCo_2O_4$ (−0.19 eV), indicating that its activation of H_2O was largely enhanced. The H_2O dissociation energy barrier was reduced from 0.32 eV to 0.14 eV, effectively promoting the generation of *H active species. Meanwhile, the ΔG of H_2 generation on the surface of Mn–$CuCo_2O_{4-x}$ ($\Delta G = 0.38$ eV) showed a significant positive shift compared with that of $CuCo_2O_4$ ($\Delta G = 0.07$ eV), suggesting that Ov significantly inhibited the generation of H_2 by the coupling of *H. In conclusion, Ov can lower the hydrogenation barrier of *NO → *HNO, accelerating the H_2O dissociation and inhibiting the HER side reaction, thereby enhancing selective NO_3^--to-NH_3 conversion.

After identifying *NO → *HNO as the RDS, density functional theory (DFT) deciphered orbital interaction mechanisms between $CuCo_2O_4$/Mn–$CuCo_2O_{4-x}$ and reaction intermediates. Density of states analysis of *NO and *HNO intermediates revealed pronounced spin asymmetry in *NO across spin-up/down channels, contrasting with spin symmetry in *HNO (Fig. 4g). This shift in spin configuration revealed a spin rearrangement phenomenon occurring during the reaction, which essentially stems from the pairing process of unpaired electrons. Differential charge density analysis revealed that *NO adsorbed on the surface of Mn–$CuCo_2O_{4-x}$ ($0.28|e|$) had a higher electron transfer number compared with $CuCo_2O_4$ ($0.16|e|$), suggesting that Ov intensified the interfacial electron transfer process and the bonding tendency to the *NO intermediates was stronger (Fig. 4h).[43] Meanwhile, enhanced *NO adsorption was observed on Mn–$CuCo_2O_{4-x}$ (−1.96 eV) relative to $CuCo_2O_4$ (−1.32 eV). Thus, the spin-state transition promoted *NO adsorption on catalysts, corroborated by projected density of states (PDOS) analysis. Fig. 4i reveals a significant overlap region between the hybridization of the Co-3d orbitals in Mn–$CuCo_2O_{4-x}$ and the N-2p orbitals of *NO and the hybridization energy intervals skewed towards the Fermi energy level, suggesting the existence of a stronger orbital interaction in Mn–$CuCo_2O_{4-x}$ and *NO.[43] Furthermore, Mn–$CuCo_2O_{4-x}$ enhanced *NO hydrogenation by stabilizing critical *HNO intermediates, which can be illustrated by the fact that *HNO adsorbed on Mn–$CuCo_2O_{4-x}$ exhibited a larger electron transfer number and a more negative adsorption energy than $CuCo_2O_{4-x}$.[44] Based on the previous analysis of the orbital configuration of the Co high spin-state ($t_{2g}^4e_g^2$), its $d_{xz}/d_{yz}/d_{z^2}$ orbitals can form directional hybridization with the σ/π^* antibonding orbitals of *NO, whereas the d_{xy} and $d_{x^2-y^2}$ orbitals are excluded from the effective coupling regime due to symmetry mismatch.[43,45] In this hybridization, the d_{z^2} orbitals of Co can accept electron occupation from the σ orbitals while the d_{xz}/d_{yz} orbitals feed electrons back to the π* orbitals. This Co 3d ($d_{xz}/d_{yz}/d_{z^2}$)–*NO 2p asymmetrical orbital hybridization enhanced the adsorption of *NO intermediates and weakened the N–O bond, thereby facilitating *NO hydrogenation to *HNO (Fig. 4j). The unique catalytic properties of $CuCo_2O_4$ and Mn–$CuCo_2O_{4-x}$ can also be illustrated by the magnetic moment of Co orbitals. The magnetic moment of Co increased from $1.356\mu_B$ to $1.661\mu_B$ after the introduction of Ov (Fig. 4k). The elevated magnetic moment is directly associated with the elevated occupancy of the HS state of Co, and the increase in the number of its unpaired electrons facilitates electron exchange between the active site and *NO, accelerating the kinetics of *NO hydrogenation. To summarize, by combining experimental characterization with DFT calculations, we revealed that the elevation of the internal Co spin state in the Cu–Co bimetallic active sites can further enhance the Cu–Co synergistic catalysis through the role of orbital hybridization.

4. Conclusions

In summary, the spin-state of Co^{3+} in spinel $CuCo_2O_4$ was modulated by an Mn doping-driven Ov strategy, and the controllable transition from the LS state to the HS state was successfully realized, significantly enhancing the Cu–Co bimetallic synergistic catalysis. Experiments and DFT revealed that the HS state Co^{3+} can optimize the adsorption of the key intermediate *NO and hydrogenation step *via* enhancing the asymmetric hybridization of the Co 3d ($d_{xz}/d_{yz}/d_{z^2}$)–*NO 2p orbitals, thus accelerating the eNO_3^-RR kinetic process. Mn–$CuCo_2O_{4-x}$/GAs demonstrated superior electrocatalytic performance, achieving an NH_3 yield rate of 2.14 mg h^{-1} cm^{-2} and a faradaic efficiency of 98.37% at −0.6 V *vs.* RHE, outperforming both Co_3O_4/GAs and $CuCo_2O_4$/GAs, as well as previously reported catalysts. This work proposes the first theoretical correlation between spin-state modulation and bimetallic synergistic catalysis, offering a new avenue for the design of high-performance catalytic systems for the deep purification of water pollutants and resource recovery.

Author contributions

Ke Wang and Tong Zhao: data curation and writing – original draft. Hou Wang and Shiyu Zhang: investigation. Rupeng Wang: formal analysis. Meng Wang: writing – review & editing. Zixiang He: supervision. Shih-Hsin Ho: funding acquisition.

Conflicts of interest

There are no conflicts to declare.

Data availability

The authors confirm that the data supporting the findings of this study are available within the article and its supplementary information (SI). Supplementary information is available. See DOI: **https://doi.org/10.1039/d5sc06823a**.

Acknowledgements

This work received research funding from the National Natural Science Foundation of China (No. 52070057), State Key Laboratory of Urban–Rural Water Resources and Environment (Harbin Institute of Technology) (No. 2025DX06), and State Key Laboratory of Water Pollution Control and Green Resource Recycling Foundation (No. PCRRF25010).

References

1 J. G. Chen, R. M. Crooks, L. C. Seefeldt, K. L. Bren, R. M. Bullock, M. Y. Darensbourg, P. L. Holland, B. Hoffman, M. J. Janik, A. K. Jones, M. G. Kanatzidis, P. King, K. M. Lancaster, S. V. Lymar, P. Pfromm, W. F. Schneider and R. R. Schrock, *Science*, 2018, **360**, eaar6611.
2 Y. Wang, C. Wang, M. Li, Y. Yu and B. Zhang, *Chem. Soc. Rev.*, 2021, **50**, 6720–6733.
3 P. H. van Langevelde, I. Katsounaros and M. T. M. Koper, *Joule*, 2021, **5**, 290–294.
4 Y. Xue, Q. Yu, Q. Ma, Y. Chen, C. Zhang, W. Teng, J. Fan and W.-x. Zhang, *Environ. Sci. Technol.*, 2022, **56**, 14797–14807.
5 W. Duan, Y. Chen, H. Ma, J.-F. Lee, Y.-J. Lin and C. Feng, *Environ. Sci. Technol.*, 2023, **57**, 3893–3904.
6 S. Han, H. Li, T. Li, F. Chen, R. Yang, Y. Yu and B. Zhang, *Nat. Catal.*, 2023, **6**, 402–414.
7 F.-Y. Chen, Z.-Y. Wu, S. Gupta, D. J. Rivera, S. V. Lambeets, S. Pecaut, J. Y. T. Kim, P. Zhu, Y. Z. Finfrock, D. M. Meira, G. King, G. Gao, W. Xu, D. A. Cullen, H. Zhou, Y. Han, D. E. Perea, C. L. Muhich and H. Wang, *Nat. Nanotechnol.*, 2022, **17**, 759–767.
8 K. Fan, W. Xie, J. Li, Y. Sun, P. Xu, Y. Tang, Z. Li and M. Shao, *Nat. Commun.*, 2022, **13**, 7958.
9 K. Wang, R. Mao, R. Liu, J. Zhang, H. Zhao, W. Ran and X. Zhao, *Nat. Mater.*, 2023, **1**, 1068–1078.
10 S. Zhang, J. Wu, M. Zheng, X. Jin, Z. Shen, Z. Li, Y. Wang, Q. Wang, X. Wang, H. Wei, J. Zhang, P. Wang, S. Zhang, L. Yu, L. Dong, Q. Zhu, H. Zhang and J. Lu, *Nat. Commun.*, 2023, **14**, 3634.
11 G.-F. Chen, Y. Yuan, H. Jiang, S.-Y. Ren, L.-X. Ding, L. Ma, T. Wu, J. Lu and H. Wang, *Nat. Energy*, 2020, **5**, 605–613.
12 H. Liu, X. Lang, C. Zhu, J. Timoshenko, M. Rüscher, L. Bai, N. Guijarro, H. Yin, Y. Peng, J. Li, Z. Liu, W. Wang, B. R. Cuenya and J. Luo, *Angew. Chem., Int. Ed.*, 2022, **61**, e202202556.
13 W. He, J. Zhang, S. Dieckhöfer, S. Varhade, A. C. Brix, A. Lielpetere, S. Seisel, J. R. C. Junqueira and W. Schuhmann, *Nat. Commun.*, 2022, **13**, 1129.
14 J.-Y. Fang, Q.-Z. Zheng, Y.-Y. Lou, K.-M. Zhao, S.-N. Hu, G. Li, O. Akdim, X.-Y. Huang and S.-G. Sun, *Nat. Commun.*, 2022, **13**, 7899.
15 Z. Ren, K. Shi, Z. Meng, M. D. Willis and X. Feng, *ACS Energy Lett.*, 2024, **9**, 3849–3858.
16 R. Yan, H. Yin, X. Zuo, W. Peng, X. Zhu, L. Shi, J. Hou, D. Wang, F. Ye, J. Li, B. Mao and C. Hu, *Appl. Catal., B*, 2025, **361**, 124609.
17 Z. Gu, Y. Zhang, X. Wei, Z. Duan, Q. Gong and K. Luo, *Adv. Mater.*, 2023, **35**, 2303107.
18 Y. Zhou, R. Duan, H. Li, M. Zhao, C. Ding and C. Li, *ACS Catal.*, 2023, **13**, 10846–10854.
19 C. Zhou, C.-Z. Yuan, F. Jing, C.-H. Li, H. Zhao, Y. Sun and W. Yuan, *J. Energy Chem.*, 2025, **106**, 142–150.
20 Y. Xie, Y. Feng, S. Zhu, Y. Yu, H. Bao, Q. Liu, F. Luo and Z. Yang, *Adv. Mater.*, 2025, **37**, 2414801.
21 M. Duan, C. Huang, G. Zhang, H. Shi, P. Zhang, L. Li, T. Xu, Z. Zhao, Z. Fu, J. Han, Y. Xu and X. Ding, *Angew. Chem., Int. Ed.*, 2024, **63**, e202318924.
22 L. Zhao, C. Xin, C. Yu, Y. Xing, Z. Wei, H. Zhang, T. Fei, S. Liu, H. Zhang and T. Zhang, *InfoMat*, 2025, **7**, e12634.
23 M. Xu, H. Zhou, X. Lv, Y. Fang, X. Tu, F. Wang, Q. Han, X. Wang and G. Zheng, *Adv. Mater.*, 2025, 2505286.
24 J. Qi, Q. Bai, X. Bai, H. Gu, S. Lu, S. Chen, Q. Li, X. Yang, J. Wang and L. Wang, *Adv. Sci.*, 2025, 2503665.
25 S. Zhang, W. Zhao, J. Liu, Z. Tao, Y. Zhang, S. Zhao, Z. Zhang and M. Du, *Adv. Sci.*, 2024, **11**, 2407301.
26 J. Ding, Z. Wei, F. Li, J. Zhang, Q. Zhang, J. Zhou, W. Wang, Y. Liu, Z. Zhang, X. Su, R. Yang, W. Liu, C. Su, H. B. Yang, Y. Huang, Y. Zhai and B. Liu, *Nat. Commun.*, 2023, **14**, 6550.
27 J. Qiao, C. Lu, L. Kong, J. Zhang, Q. Lin, H. Huang, C. Li, W. He, M. Zhou and Z. Sun, *Adv. Funct. Mater.*, 2024, **34**, 2409794.
28 H. Xue, J. Wang, H. Cheng, H. Zhang, X. Li, J. Sun, X. Wang, L. Lin, Y. Zhang, X. Liao and Y. He, *Appl. Catal., B*, 2024, **353**, 124087.
29 Z. Huang, Y. Liang, Z. Wu, Y. Kong, M. Bai, M. Li, B. Hong, T. Huang, S. Huang, H. Chen and S. Zhang, *Adv. Mater.*, 2025, **37**, 2410318.
30 Y.-X. Zhang, Y.-D. Li, A.-K. Du, Y. Wu and J.-B. Zeng, *J. Mater. Sci. Technol.*, 2024, **173**, 114–120.

31 J. Geltmeyer, G. Vancoillie, I. Steyaert, B. Breyne, G. Cousins, K. Lava, R. Hoogenboom, K. De Buysser and K. De Clerck, *Adv. Funct. Mater.*, 2016, **26**, 5987–5996.

32 K. Liu, X. Gao, C.-X. Liu, R. Shi, E. C. M. Tse, F. Liu and Y. Chen, *Adv. Energy Mater.*, 2024, **14**, 2304065.

33 Y. Chen, Q. Li, R. Su, Y. Gao, N. An, Y. Rong, X. Xu, D. Ma, Y. Wang and B. Gao, *Water Res.*, 2025, 123765.

34 H. Lin, J. Wei, Y. Guo, Y. Li, X. Lu, C. Zhou, S. Liu and Y.-y. Li, *Adv. Funct. Mater.*, 2024, **34**, 2409696.

35 X. Guo, W. Cai, Y. Zhuo and S. Liu, *Appl. Catal., B*, 2025, **373**, 125354.

36 L. Wu, Q. Wu, Y. Han, D. Zhang, R. Zhang, N. Song, X. Wu, J. Zeng, P. Yuan, J. Chen, A. Du, K. Huang and X. Yao, *Adv. Mater.*, 2024, **36**, 2401857.

37 K. Wang, T. Zhao, N.-Q. Ren and S.-H. Ho, *Water Res.*, 2024, **265**, 122304.

38 Q. Deng, H. Li, K. Pei, L. W. Wong, X. Zheng, C. S. Tsang, H. Chen, W. Shen, T. H. Ly, J. Zhao and Q. Fu, *ACS Nano*, 2024, **18**, 33718–33728.

39 M. Xie, G. Zhu, H. Yang, B. Liu, M. Li, C. Qi, L. Wang, W. Jiang, P. Qiu and W. Luo, *Adv. Energy Mater.*, 2024, **14**, 2401717.

40 J. Li, H. Li, K. Fan, J. Y. Lee, W. Xie and M. Shao, *Chem Catal.*, 2023, **3**, 100638.

41 Y. Huang, C. He, C. Cheng, S. Han, M. He, Y. Wang, N. Meng, B. Zhang, Q. Lu and Y. Yu, *Nat. Commun.*, 2023, **14**, 7368.

42 J. Ni, J. Yan, F. Li, H. Qi, Q. Xu, C. Su, L. Sun, H. Sun, J. Ding and B. Liu, *Adv. Energy Mater.*, 2024, **14**, 2400065.

43 J. Liang, S. Deng, Z. Li, M. Zhou, S. Wang, Y. Su, S. Yang and H. Li, *Adv. Mater.*, 2025, **37**, 2418828.

44 J. Dai, Y. Tong, L. Zhao, Z. Hu, C.-T. Chen, C.-Y. Kuo, G. Zhan, J. Wang, X. Zou, Q. Zheng, W. Hou, R. Wang, K. Wang, R. Zhao, X.-K. Gu, Y. Yao and L. Zhang, *Nat. Commun.*, 2024, **15**, 88.

45 Y. Sun, S. Sun, H. Yang, S. Xi, J. Gracia and Z. J. Xu, *Adv. Mater.*, 2020, **32**, 2003297.